

www.acsabm.org Article

Extrusion 3D Printing of Porous Silicone Architectures for Engineering Human Cardiomyocyte-Infused Patches Mimicking Adult Heart Stiffness

Tony Thomas, Alberto S. Rubfiaro, Pranjal Nautiyal, Roy Brooks, Darryl Dickerson, Jin He, and Arvind Agarwal*



Cite This: ACS Appl. Bio Mater. 2020, 3, 5865-5871

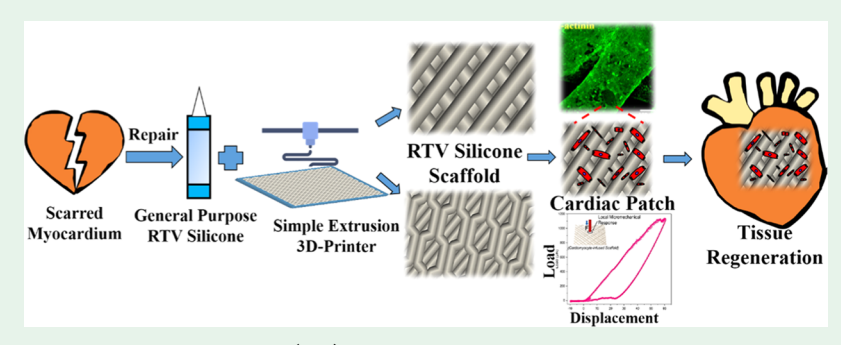


ACCESS

Metrics & More

Article Recommendations

Supporting Information



ABSTRACT: Cardiac patches, three-dimensional (3D) constructs of polymer scaffold and heart muscle cells, have received widespread attention for regenerative therapy to repair damaged heart tissue. The implanted patches should mimic the micromechanical environment of native myocardium for effective integration and optimum mechanical function. In this study, we engineered compliant silicone scaffolds infused with cardiomyocytes (CMs) differentiated from human-induced pluripotent stem cells. Porous scaffolds are fabricated by extrusion 3D printing of room-temperature-vulcanized (RTV) silicone rubber. The stiffness and strength of scaffolds are tailored by designing a polymer strand arrangement during 3D printing. Single-strand scaffold design is found to display a tensile Young's modulus of ~280 kPa, which is optimum for supporting CMs without impairing their contractility. Uniform distribution of cells in the scaffold is observed, ascribed to 3D migration facilitated by interconnected porous architecture. The patches demonstrated synchronized contraction 10 days after seeding scaffolds with CMs. Indentation measurements reveal that the contracting cell-scaffold patches display local moduli varying from ~270 to 530 kPa, which covers the upper spectrum of the stiffness range displayed by the human heart. This study demonstrates the effectiveness of a porous 3D scaffold composed of flexible silicone rubber for CMs percolation, supporting a contractile activity, and mimicking native heart stiffness.

KEYWORDS: 3D printing, RTV silicone, porous scaffold, cardiac patch, hiPSC, tensile strength

1. INTRODUCTION

Cardiovascular disorders can cause irreversible damage to the heart muscle, impairing cardiac function, and causing heart failure.¹ The heart muscle cells, known as cardiomyocytes (CMs), are believed to be nonproliferative.² As a result, when the heart is damaged, cells that replace dead CMs produce a rigid scar tissue that cannot contract, creating an undesirable mechanical mismatch and leading to reduced cardiac output over time.³ Cardiac regenerative therapy, making use of cells and biomaterials, has been explored for the functional repair of damaged areas with different degrees of success.⁴ Direct administration of cells to the damage site results in a low engraftment rate, limiting the effectiveness of the treatments.^{5,6} To enhance retention of cells, cardiac patches composed of a biomaterial scaffold seeded with cells can be implanted into the damaged areas.^{1,4} Cardiac patches support and revitalize the

tissue by supplying cells and growth factors, restoring functionality. The design and fabrication of patches should take into consideration cytocompatibility, mechanical properties, scalability, and morphological resemblance to native myocardium for effective integration and therapeutic effect.⁷

Biomaterial scaffolds used for cardiac patches must have physical properties that promote cell infiltration and differentiation, support extracellular matrix deposition, provide biochemical cues to define cell characteristics, and permit the

Received: May 16, 2020 Accepted: July 27, 2020 Published: July 28, 2020





efficient flow of nutrients and metabolic waste.8-12 Many of these properties can be tuned by employing 3D printing for scaffold manufacturing. Three-dimensional (3D) printing provides manufacturing flexibility to mimic tissue microarchitectures with extraordinary precision to accommodate fully mature cardiomyocytes that are typically cylindrical and measuring $60-140~\mu m$ in length and $17-25~\mu m$ in diameter. Three-dimensional porous architecture should accommodate the high-aspect-ratio cardiomyocytes (length to diameter ratio 5:1), along with the material characteristics that determine the mechanical properties of the scaffold. The elastic modulus of the human heart is reported to vary from ~20 to 500 kPa. 1,7,16 To print compliant scaffolds suitable for supporting contracting CMs, we used a room-temperaturevulcanized (RTV) silicone rubber, which displays a combination of biocompatibility, biodurability, chemical stability, and ease of printing. 17-19 A facile extrusion 3D printing approach is employed in this study to fabricate porous RTV scaffolds.

In the last decade, CMs differentiated from human-induced pluripotent stem cells (hiPSCs) have shown promise for transplantation and enhancement of cardiac mechanical function. Although the morphology and function of hiPSC-derived CMs resemble fetal CMs, 20,21 recent successes with electromechanical stimulation demonstrate the feasibility of advanced maturation to realize adultlike characteristics. It is expected that upon maturation, hiPSC-derived CMs within an appropriate biomaterial scaffold will mimic native human heart tissue. Therefore, we infused the compliant RTV scaffolds with hiPSC-CMs to fabricate cardiac patches. This study examines the cell infiltration, migration, attachment, and proliferation in the printed scaffold. The cell-infused RTV scaffolds displayed synchronous beating and local elastic moduli mimicking human heart stiffness, demonstrating the potential for use as a cardiac patch for heart tissue regeneration.

2. EXPERIMENTAL SECTION

2.1. 3D Printing. An extrusion type 3D printer was used for this study to demonstrate how a relatively simple 3D printing system can be used for cardiac tissue engineering (TE). CAD models were generated for a series of different scaffold designs with variations in pore shape and pore size described in the Results section. Extrusion of the silicone-based scaffold material was performed using a Hyrel-System 30M equipped with a high torque printing head (VCD 400). The extrusion nozzle was 0.84 mm in diameter (inner diameter). Each scaffold consisted of six layers of 0.35 mm each. A constant print speed of 35 mm s⁻¹ was maintained for all of the printing operations. Readily available RTV silicone (SILASEAL, Professional Grade 100% RTV Silicone, Indianapolis) was used in its original composition throughout this study. This is a clear silicone that comes under the category of silicone elastomers. They are a mixture of ethyltriacetoxysilane and methyltriacetoxysilane, and their mixture ratio is proprietary to SILASEAL. Each 3D-printed scaffold was cured in the air for 24 h to ensure complete polymerization.

2.2. Mechanical Characterization. To evaluate the tensile mechanical properties of the scaffold, dog-bone samples conforming to the ASTM D638 standard were 3D printed. A minimum of three dog-bone samples of each scaffold design was tested in an MTS Criterion Model 41 machine to obtain average mechanical property values.

The indentation technique was used to perform mechanical measurements on CMs (in the scaffolds). A high-displacement span indenter (BioSoft, Bruker), with a piezoactuation limit exceeding 150 μ m, was employed to capture the aggregate response of the seeded cell clusters. The indenter head was mounted on an inverted optical microscope (Zeiss) to image the cells prior to indentation. A five-step indentation test was programmed, comprising of approach, load, hold,

unload, and retract segments. A 50 μ m conospherical probe was used for these experiments. The cells were submerged in phosphate-buffered solution (PBS) media throughout the mechanical tests. The buoyancy correction was applied to the force response using the readings captured during the approach segment. The buoyancy effects can be prominent during the mechanical measurements of submerged samples and should be taken into consideration. ²⁰

2.3. Tissue Engineering Study. 2.3.1. Scaffold Sterilization. The scaffolds (initial size 2×2 cm) were cropped to an area of 1×1 cm and rinsed with deionized (DI) water. Scaffolds were immersed in 70% of ethanol for 1 day. To enhance the adhesion of organic components, the scaffolds were treated in a Harrick plasma cleaner (PDC-001) for 10 min to produce a hydrophilic surface. This step was followed by a treatment with 1% 3-aminopropyl triethoxysilane (APTES, Sigma) for 30 min, then immersed in 0.5% of glutaraldehyde for 30 min at room temperature. Afterward, scaffolds were cleaned with 70% of ethanol, followed by rinsing in distilled water and dried under UV light.

2.3.2. Culture and CM Differentiation of hiPSCs. hiPSCs (human iPSCs from reprogrammed fibroblasts, GM23338) were purchased from Coriell Institute for Medical Research (NJ) and grown on Matrigel-coated plates (BD Biosciences) in stem basal medium (mTeSR1, STEMCELL Technologies). $^{23-25}$ When hiPSCs reached 80–90% confluence, they were dissociated with Accutase (Invitrogen). On day 0, hiPCSs were treated with 12 μ M of a selective inhibitor of glycogen synthase kinase 3 (CHIR99021, Tocris) diluted in RPMI/B27-insulin with media changed every day up to day 3. On day 3, hiPSCs were treated with 5 μ M IWP4 (Tocris) mixed with RPMI/B27-insulin for one day, inhibiting Wnt/ β -catenin signal transduction pathway. From day 9, hiPSCs were maintained in RPMI/B27 containing insulin with regular medium change. Spontaneous contractions were observed between 9th and 12th day after starting the differentiation process.

2.3.3. Seeding hiPSC-Derived CMs into Scaffold. RTV scaffolds were treated with 10 μ g mL⁻¹ of human fibronectin (Corning) in a sterile phosphate-buffered solution (1 × PBS, Gibco) for 1 h at 37 °C and rinsed with sterile 1 × PBS. hiPSC-derived CMs were detached from tissue culture plates by adding 0.25% trypsin-EDTA (Gibco) at 37 °C for 10 min. The detached hiPSC-derived CMs were immediately placed on the scaffolds at a density of 6 × 10⁵ cells cm⁻². The hiPSC-derived CMs were cultured in the scaffold in RPMI/B27 containing insulin and 2% of fetal bovine serum (FBS, Gibco), and the medium was replaced every other day. RTV scaffolds seeded with hiPSC-derived CMs were cultured for up to 21 days.

2.3.4. Immunostaining. At days 0, 3, 7, 10, 15, and 20 after cell seeding, immunohistochemical analysis was performed on RTV scaffold samples. The scaffolds were immersed in 4% of paraformaldehyde for 20 min, blocked and permeabilized with 0.2% of TritonX-100 and 1% of BSA in 1 \times PBS for 20 min at room temperature. Cells were stained overnight with the primary antibody, antisarcomeric α -actinin (abcam, 1:200 dilution). Samples were incubated with goat antimouse secondary antibody Alexa-488 for 60 min (abcam, 1:200 dilution), followed by 10 min incubation with 4 $^{\prime}$,6-diamidino-2-phenylindole (DAPI) (Invitrogen, 30 nM).

2.3.5. Imaging. Field emission scanning electron microscopy (FE-SEM JEOL JSM-6330F, JEOL Ltd. Tokyo, Japan) was employed to examine the 3D-printed scaffold. Optical microscopy (Versamet 3, Buehler, Lake Bluff, IL) was used to evaluate the pore size and area in the 3D-printed scaffold. Confocal fluorescence microscope (Nikon, A1 HD25) was used to monitor the maturation of CMs as a function of days in the scaffold.

3. RESULTS AND DISCUSSION

3.1. Scaffold Design. One of the most critical characteristics of tissue engineering (TE) scaffold is its mechanical stiffness, which is known to greatly influence cell responses including differentiation, migration, and surface adhesion. ²⁶ In this study, two scaffold designs as shown in the schematic in

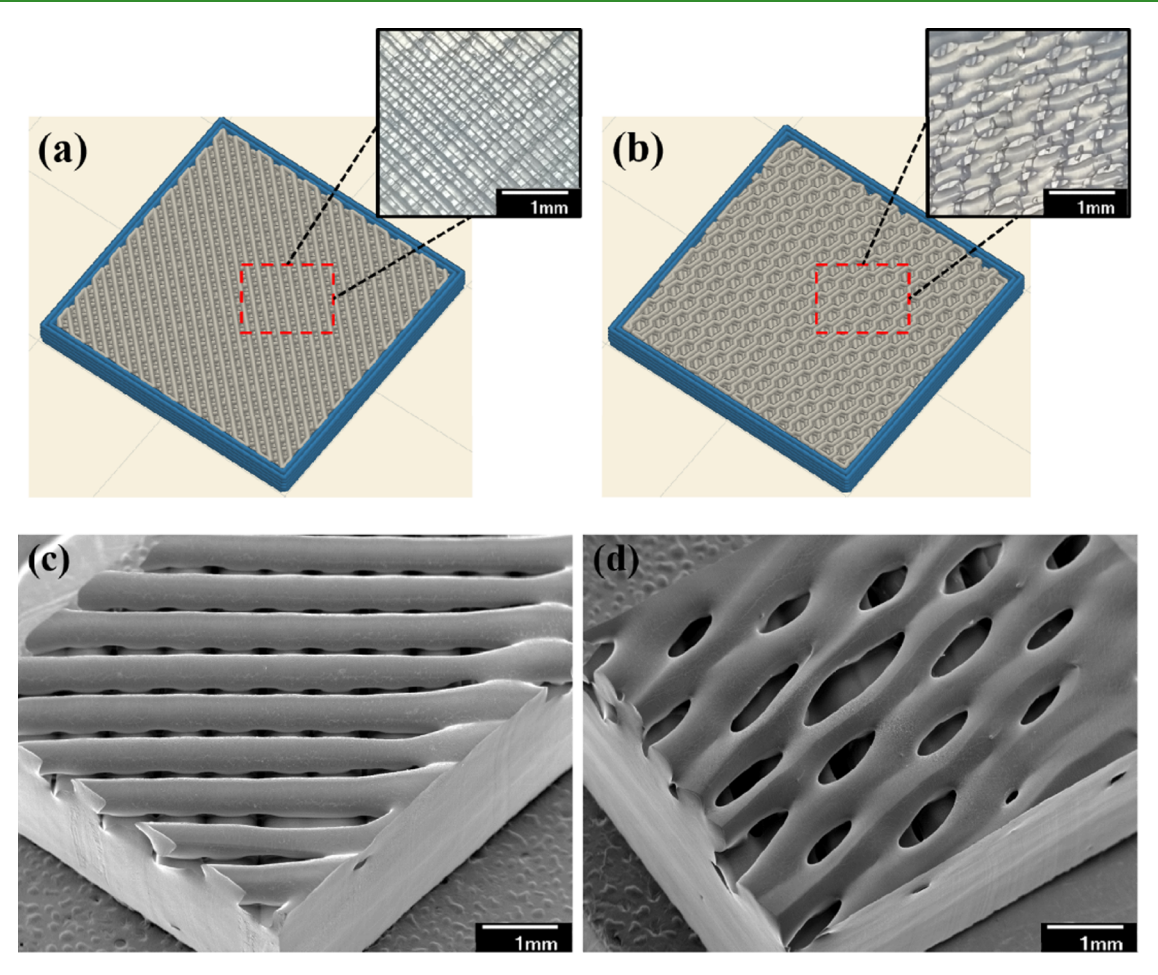


Figure 1. Scaffold designed and 3D printed in this study $(20 \times 20 \times 2 \text{ mm}^3)$. (a) and (b) Single-strand and double-strand CAD models, respectively [inset showing optical images of the scaffold design]. (c) and (d) SEM images showing the isometric view of the 3D-printed single-strand and double-strand scaffolds, respectively.

Figure 1a,b were considered to produce scaffolds of different stiffness.

The single-strand design (Figure 1a) has a simple rectangular pore (refer to the inset in Figure 1a) formed by the layers of lines 3D printed at 45° to the previous layer. In contrast, the double-strand design (Figure 1b) has an oval pore shape formed by two conjoint lines (refer to the inset in Figure 1b). Scaffolds of varying infill porosity (25, 50, 60, and 75%) were 3D printed to establish optimum pore size for cellular adhesion and migration (refer to Supporting Video 1 to see the 3D-printing process). The SEM images of single-strand (Figure 1c) and double-strand (Figure 1d) scaffolds with 50% porosity demonstrate a smooth surface finish and consistent pore morphology resulting from the 3D-printing process. For both scaffold designs at 50% infill porosity, pore sizes ranged from 100 to 200 μ m, matching values found in the literature for scaffolds used for other tissue engineering applications.^{26–28} Thus, 50% of infill porosity scaffolds were used for subsequent mechanical characterization and tissue engineering studies.

From Table 1, it can be noticed that, for the same amount of infill porosity (50%), the single-strand scaffold has more than twice the pore area as compared to the double-strand scaffold design. This will directly influence the mechanical property offered by these scaffolds.

3.2. Tensile Property. ASTM D638 standard dog-bone samples with single-strand and double-strand designs were 3D

Table 1. Pore Characterization Data

scaffold design	pore size $[\mu m]$	pore area $[\mu m^2]$
single strand	142×142	~20 000
double strand	174×50	~8700

printed to characterize the effect of the design on the mechanical properties of the scaffold.

As shown in Figure 2, a single-strand design recorded an ultimate tensile strength (UTS) of 500 ± 50 kPa, whereas a

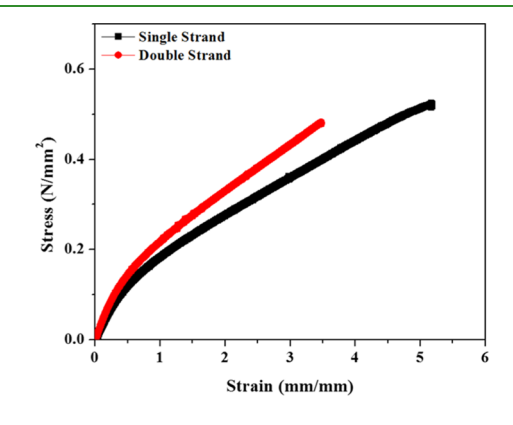


Figure 2. Stress vs strain behavior of 3D-printed single-strand and double-strand dog-bone samples.

double-strand design exhibited a UTS of 440 \pm 50 kPa. It is interesting to observe that though a single-strand design has a pore area twice that of a double-strand design, it exhibits higher tensile strength. This is because the single-strand design can withstand 37% more strain than the double-strand design before failure, substantiating the effect of the architecture in distributing the stress efficiently. The single-strand design has an elastic modulus of 280 ± 40 kPa, which is 16% lower than the double-strand design. Hence, a single-strand design provides more elasticity to the scaffold than a double-strand design. The elastic modulus of both scaffold designs is comparable with the elastic modulus of the human heart, which range from ~20 to 500 kPa. $^{1.7,8}$ The elastic modulus may be further tuned by varying the diameter of these strands.

3.3. Cell Differentiation, Seeding, and Culturing. The differentiated CMs were seeded into both the scaffolds at a density of 6×10^5 cells cm⁻² and cultured in the RPMI/B27 mixture containing insulin and 2% of FBS. Prior to seeding, the scaffolds were treated with 10 μg mL⁻¹ of human fibronectin to improve cell adhesion, to increase migration, and to promote cell—cell interaction through mechanical forces. To the authors' knowledge, this is the first study to examine RTV silicone as a scaffold for cardiac tissue engineering. The cells started beating in the patch after 5 days of seeding, demonstrating the mechanical and biological suitability of RTV silicone as a potential cardiac tissue engineering scaffold. As shown in Figure 3, cells seeded in a single-strand scaffold were

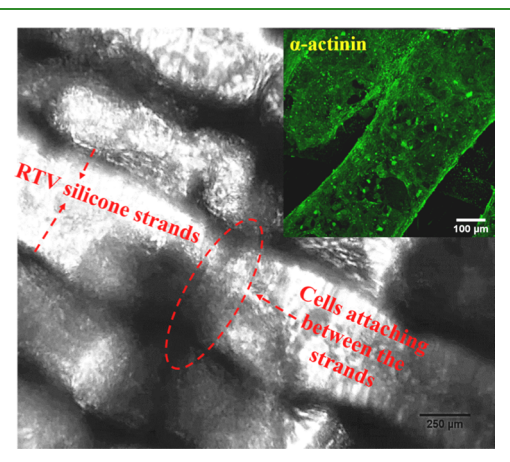


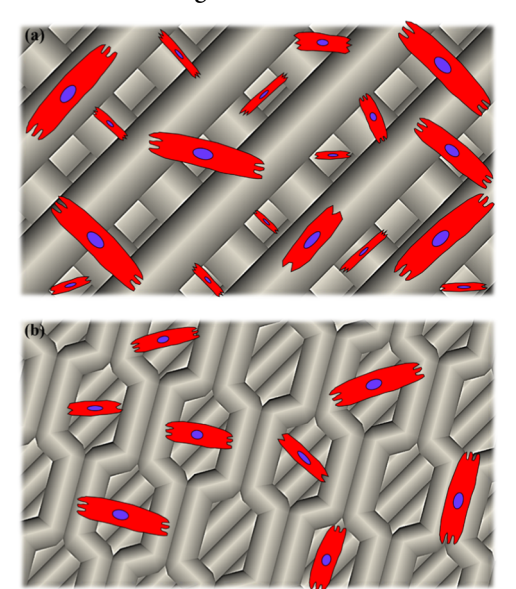
Figure 3. Optical image showing the formation of CM network between the strands of the single-strand scaffold. Inset is the confocal image of the CMs attached to the strands of the single-strand scaffold.

able to migrate across the 3D porous structure, find a suitable surface to attach, and form a cellular network to stimulate localized beating (refer to Supporting Video 2). The fluorescence confocal image in the inset of Figure 3 reveals a dense layer of CMs adhered to the circumference of the strands throughout the scaffold. Through mechanotransduction, the cells in a single-strand scaffold generated mature focal adhesions. This can only occur when scaffolds offer adequate stiffness, such that the cell can generate large forces within the scaffold to form a highly organized cytoskeleton, as shown in Figure 3 (within the red-dashed oval).²⁴

Another interesting observation was that only the cells seeded in the single-strand scaffold stimulated beating cycles. Cells seeded in the double-strand scaffold did not endure the process. Given the biochemical similarity between the scaffolds, this result suggests a strong connection between

cell viability and the physical characteristics (pore structure and mechanical stiffness) offered by the scaffold architecture. The single-strand design has a larger pore size as compared to the double-strand design (refer Table 1). As shown in the schematic in Scheme 1, the single-strand design (Scheme 1a)

Scheme 1. Schematic Showing the Effect of Interconnected Porosity in Cell Percolation. (a) Single-Strand Design and (b) Double-Strand Design



has interconnected porous layers, which facilitated cell migration and the flow of nutrients and metabolic waste within the structure. In the double-strand configuration (Figure 4b), the pores are confined and not interconnected. Moreover, only one porous layer is present across the surface in a double-strand scaffold, thereby increasing the stiffness of the scaffold. The larger pore size and lower stiffness of the single-strand scaffold promoted effective cellular migration and infiltration to stimulate cell activity. Hence, further TE results reported in this section are only on a single-strand scaffold.

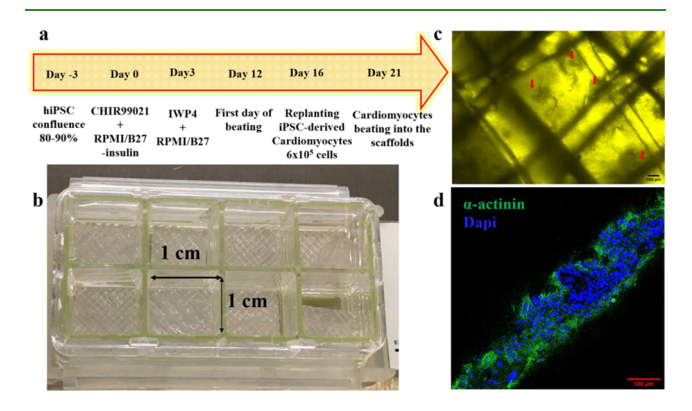


Figure 4. (a) Timeline of hiPSC monolayer differentiation and culturing in the scaffold, (b) setup showing scaffolds prepared for seeding hiPSC-derived CMs, (c) optical image showing CMs attached to the single-strand scaffold, red arrows on yellow pseudo background show clusters of hiPSC-derived CMs after day 10 of seeding, synchronized-like contraction is shown in Supporting Video 3, and (d) fluorescence confocal microscope image of a single strand showing adhesion of hiPSC-derived CMs.

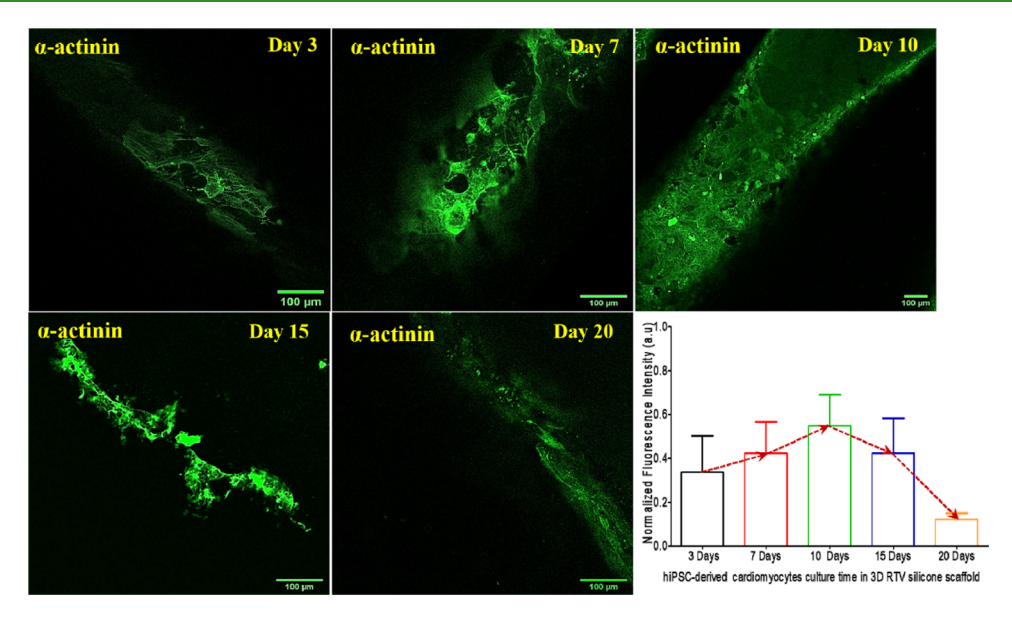


Figure 5. Confocal microscope images showing the adhesion of hiPSC-derived CMs (α -actinin, green) in the single-strand scaffold over 21 days.

A detailed study was conducted to explore the capability of the single-strand scaffold to support cell adhesion and proliferation of hiPSC-derived CMs. Figure 4a shows the experimental protocol followed in this study. The hiPSCs were differentiated through the modulation of Wnt/ β -catenin signaling that produced 85–95% CMs purity. Figure 4b shows the setup used to seed hiPSC-derived CMs into the scaffold to form the patches. The scaffolds were coated with human fibronectin to promote cell adhesion. After day 5 of seeding, the beating of individual CMs was observed. The pulse was of low frequency (43 beats per minute (BPM)) and nonsynchronized (refer Supporting Video 2), which may be due to the lack of mechanical and electrical coupling.

Figure 4c shows an optical image of the scaffold after 10 days of seeding. Here, a synchronized contraction (32 BPM, refer Supporting Video 3) can be observed. A dense network of cells is seen widespread across the 3D structure of the scaffold (represented by red arrows on the yellow pseudo-background). Fluorescence confocal microscope images (Figure 4d) reveal cells attached to all areas of the scaffold. The presence of a dense network of cells also indicates that the single-strand scaffold design promoted efficient proliferation and migration of the cells to form a cardiac patch.

Confocal microscope images (Figure 5) reveal cell attachment through the 3D structure of the scaffold over the 21-day tissue culture period. The graph showing the normalized fluorescence intensity change over time suggests that the maximum confluence density of cells was reached at day 10 after seeding and slowly decayed after that for the rest of the time. This is likely due to the change in the elastic properties of the environment (extracellular matrix, fibronectin) that might disrupt the mechanical coupling and impair the cell—cell interaction leading to termination in the contraction term with the loss of cells. ³¹ Nevertheless, the cellular study sheds light on the optimum number of days required to obtain a cardiac patch with a maximum density of healthy beating cells.

3.4. Local Micromechanical Response of Seeded CMs. An indentation test was performed on the cardiac cells attached in the scaffold to assess their stiffness. A characteristic indentation force—displacement curve captured from different regions in the patch is shown in Figure 6. The indenter probe

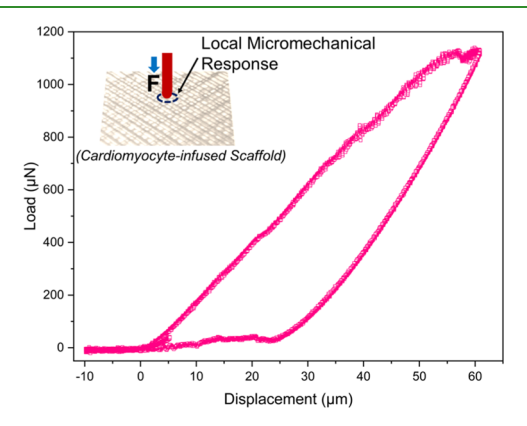


Figure 6. Load displacement curve obtained by the indentation test on live cardiac tissue attached to the scaffold. The inset shows a graphical representation of the indenter on the cardiac patch to measure the local mechanical properties.

penetrated up to 60 μ m deep inside the patch. The samples displayed elastic—plastic deformation behavior, with about \sim 60% immediate recovery, as the indenter was retracted. Since the pore size in the single-strand scaffold is only \sim 140 μ m, the force—displacement data captured by the micro-indentation technique is expected to be an aggregate response from the CMs and the silicone strands supporting the cell network.

The elastic modulus of the attached CMs was obtained by fitting the loading curve using the Hertz model

$$P = \frac{4E}{3(1 - v^2)} \sqrt{R} \,\delta^{3/2} \tag{1}$$

where P is the indentation force, δ is the indentation displacement, R is the indenter tip radius, v is the Poisson's ratio, and E is the elastic modulus of the sample. A Poisson's ratio of 0.4 was used for the calculations. The elastic modulus calculated using the Hertz model displayed location-specific variations: from a minimum of 274.9 kPa to a maximum of 532.1 kPa. These values represent the local stiffness of CMs attached to the single-strand scaffold. It is recommended that the mechanical properties of biomaterials used for cardiac TE should mimic the mechanics of the native heart. The elastic

modulus of the native human heart typically varies from 20 to 500 kPa. 1,7,16 Therefore, it is promising that the local modulus values of CMs-scaffold patches fabricated in this work are within this range. Our findings support the feasibility of employing RTV silicone as a scaffold material to fabricate cardiac patches using a simple extrusion type 3D-printing technique. Though RTV silicone is a biocompatible and noncytotoxic material, to realize it as an ideal material for a cardiac patch, future work will be directed to study its biodegradability.

4. CONCLUSIONS

In this study, a novel 3D printed rubber-based silicone scaffold was fabricated and characterized for use in cardiac tissue engineering. The RTV scaffold has been tailored to provide interconnected porosity while mimicking the microarchitecture and mechanical properties of the native myocardium. These properties were tuned by incorporating multiple silicone strands. Porous 3D-printed single-strand silicone scaffold yielded a stiffness of 280 \pm 40 kPa, which is comparable to the stiffness of the human myocardium. hiPSC-derived CMs adhered efficiently to the scaffold and multiplied to form a cardiac patch with dense CM network throughout the scaffold. These results suggest that 3D-printed RTV silicone scaffolds seeded with hiPSCs have excellent potential to become functional cardiac patches to treat myocardial infraction at the accelerated time, as the patches exhibited synchronized beating and maximum cell density after 10 days of maturation in the scaffold.

ASSOCIATED CONTENT

Supporting Information

The Supporting Information is available free of charge at https://pubs.acs.org/doi/10.1021/acsabm.0c00572.

Video 1: Time-lapse of the extrusion 3D printing of RTV silicone scaffold (MP4)

Video 2: The nonsynchronous beating of cardiomyocytes in the single-strand scaffold after 5 days of maturation (MP4)

Video 3: Synchronous beating of cardiomyocytes in the single-strand scaffold after 10 days of maturation (MP4)

AUTHOR INFORMATION

Corresponding Author

Arvind Agarwal — Department of Mechanical and Materials Engineering, Florida International University, Miami, Florida 33174, United States; orcid.org/0000-0002-7052-653X; Email: agarwala@fiu.edu

Authors

Tony Thomas – Department of Mechanical and Materials Engineering, Florida International University, Miami, Florida 33174, United States

Alberto S. Rubfiaro — Department of Physics, Biomolecular Science Institute, Florida International University, Miami, Florida 33199, United States

Pranjal Nautiyal — Department of Mechanical and Materials Engineering, Florida International University, Miami, Florida 33174, United States

Roy Brooks – Department of Mechanical Engineering, Universidad Ana G. Mendez, Recinto de Gurabo 00777, Puerto Rico Darryl Dickerson – Department of Mechanical and Materials Engineering, Florida International University, Miami, Florida 33174, United States

Jin He − Department of Physics, Biomolecular Science Institute, Florida International University, Miami, Florida 33199, United States; orcid.org/0000-0002-2633-9809

Complete contact information is available at: https://pubs.acs.org/10.1021/acsabm.0c00572

Notes

The authors declare no competing financial interest.

ACKNOWLEDGMENTS

We would like to acknowledge the Engineering Research Centers Program of the National Science Foundation under NSF Cooperative Agreement No. EEC-1647837.

REFERENCES

- (1) Reis, L. A.; Chiu, L. L.; Feric, N.; Fu, L.; Radisic, M. Biomaterials in myocardial tissue engineering. *J. Tissue Eng. Regener. Med.* **2016**, *10*, 11–28.
- (2) Sutton, M.; Sharpe, N. Left ventricular remodeling after myocardial infarction: pathophysiology and therapy. *Circulation* **2000**, *101*, 2981–2988.
- (3) Laflamme, M.; Murry, C. Regenerating the heart. *Nat. Biotechnol.* **2005**, 23, 845–856.
- (4) Zhang, J.; Zhu, W.; Radisic, M.; Vunjak-Novakovic, G. Can we engineer a human cardiac patch for therapy? *Circ. Res.* **2018**, *123*, 244–265.
- (5) Yanamandala, M.; Zhu, W.; Garry, D. J.; Kamp, T.; Hare, J.; Jun, H.; Yoon, Y.; Bursac, N.; Pradhu, S.; Dorn, G.; Bolli, R.; Kitsis, R.; Zhang, J. Overcoming the roadblocks to cardiac cell therapy using tissue engineering, *J. Am. Coll. Cardiol.* **2017**, 70, 766–775.
- (6) Zeng, L.; Hu, Q.; Wang, X.; Mansoor, A.; Lee, J.; Feygin, J.; Zhang, G.; Suntharalingam, P.; Boozer, S.; Mhashilkar, A.; Panetta, C.; Swingen, C.; Deans, R.; From, A.; Bache, R.; Verfaillie, C. M.; Zhang, J. Bioenergetic and functional consequences of bone marrow-derived multipotent progenitor cell transplantation in hearts with postinfarction left ventricular remodeling. *Circulation* **2007**, *115*, 1866–1875.
- (7) Kapnisi, M.; Mansfield, C.; Marijon, C.; Guex, A.; Perbellini, F.; Bardi, I.; Humphrey, E.; Puetzer, J.; Mawad, D.; Koutsogeorgis, D.; Stuckey, D.; Terracciano, C.; Harding, S.; Stevens, M. Auxetic cardiac patches with tunable mechanical and conductive properties toward treating myocardial infarction,. *Adv. Funct. Mater.* **2018**, 28, No. 1800618.
- (8) Nukavarapu, S.; Dorcemus, D. Osteochondral tissue engineering: current strategies and challenges. *Biotechnol. Adv.* **2013**, *31*, 706–721.
- (9) Li, X.; Huang, Y.; Zheng, L.; Liu, H.; Niu, X.; Huang, J.; Zhao, F.; Fan, Y. Effect of substrate stiffness on the functions of rat bone marrow and adipose tissue derived mesenchymal stem cells in vitro. *J. Biomed. Mater. Res. A* **2013**, *102*, 1092–1101.
- (10) Li, X.; Fan, Y.; Watari, F. Current investigations into carbon nanotubes for biomedical application. *Biomed. Mater.* **2010**, *5*, No. 22001.
- (11) Brown, T. D. Techniques for mechanical stimulation of cells in vitro: a review. *J. Biomech.* **2000**, 33, 3–14.
- (12) Leor, J.; Amsalem, Y.; Cohen, S. Cells, scaffolds, and molecules for myocardial tissue engineering. *Pharmacol. Ther.* **2005**, *105*, 151–163.
- (13) Tracy, R. E.; Sander, G. E. Histologically Measured Cardiomyocyte Hypertrophy Correlates with Body Height as Strongly as with Body Mass Index. *Cardiol. Res. Pract.* **2011**, 2011, No. 658958. (14) Gerdes, A.; Kellerman, S.; Moore, J.; Muffly, K.; Clark, L.; Reaves, P.; Malec, K.; Mckeown, P.; Scocken, D. Structural remodeling of cardiac myocytes in patients with ischemic cardiomyopathy. *Circulation* **1992**, 426–430.

- (15) Yang, X.; Pabon, L.; Murry, C. Engineering Adolescence. Circ. Res. 2014, 114, 511–523.
- (16) Silvestri, A.; Boffito, M.; Sartori, S.; Ciardelli, G. Biomimetic materials, and scaffolds for myocardial tissue regeneration. *Macromol. Biosci.* **2013**, *13*, 984–1019.
- (17) Vondrácek, P.; Dolezel, B. Biostability of medical elastomers: a review. *Biomaterials* **1984**, *5*, 209–214.
- (18) Vince, V.; Thil, M.; Veraart, C.; Colin, I.; Delbeke, J. Biocompatibility of platinum-metalized silicone rubber: in vivo and in vitro evaluation. *J. Biomater. Sci., Polym. Ed.* **2004**, *15*, 173–188.
- (19) Adams, S.; Ashok, A.; Kanwar, R.; Kanwar, J.; Kouzani, A. Integrated 3D printed scaffolds and electrical stimulation for enhancing primary human cardiomyocyte cultures. *Bioprinting* **2017**, *6*, 18–24.
- (20) Yang, X.; Pabon, L.; Murry, C. Engineering adolescence: maturation of human pluripotent stem cell-derived cardiomyocytes. *Cric. Res.* **2014**, *114*, 511–523.
- (21) Feric, N. T.; Radisic, M. Maturing human pluripotent stem cell-derived cardiomyocytes in human-engineered cardiac tissues. *Adv. Drug Delivery Rev.* **2016**, *96*, 110–134.
- (22) Ronaldson-Bouchard, K.; Ma, S. P.; Yeager, K.; Chen, T.; Song, L.; Sirabella, D.; Morikawa, K.; Teles, D.; Yazawa, M.; Vunjak-Novakovic, G. Advanced maturation of human cardiac tissue grown from pluripotent stem cells. *Nature* **2018**, *556*, 239–243.
- (23) Simič, R.; Mathis, C.; Spencer, N. A two-step method for rate-dependent nano-indentation of hydrogels. *Polymer* **2018**, *137*, 276–282.
- (24) Chiu, Y. C.; Cheng, M. H.; Engel, H.; Kao, S. W.; Larson, J. C.; Gupta, S.; Brey, E. M. The role of pore size on vascularization and tissue remodeling in PEG hydrogel. *Biomaterials* **2011**, *32*, 6045–6051.
- (25) Breuls, R.; Jiya, T.; Smit, T. Scaffold Stiffness Influences Cell Behavior: Opportunities for Skeletal Tissue Engineering. *Open Orthop. J.* **2008**, *29*, 103–109.
- (26) Loh, Q.; Choong, C. Three-dimensional scaffolds for tissue engineering applications: role of porosity and pore size. *Tissue Eng.*, *Part B* **2013**, *19*, 485–502.
- (27) Cao, L.; Zeller, M.; Fiore, V.; Strane, P.; Bermudez, H.; Barker, T. Phage-based molecular probes that discriminate force-induced structural states of fibronectin in vivo. *Proc. Natl. Acad. Sci. U.S.A.* **2012**, *109*, 7251–7256.
- (28) Smith, M.; Gourdon, D.; Little, W.; Kubow, K.; Eguiluz, R.; Luna, S.; Vogel, V. Force-induced unfolding of fibronectin in the extracellular matrix of living cells. *PLoS Biol.* **2007**, *5*, No. e268.
- (29) Chiou, K.; Rocks, J.; Cho, S.; Prosser, B.; Discher, D.; Liu, A.; et al. Mechanical signaling coordinates the embryonic heartbeat. *Proc. Natl. Acad. Sci. U.S.A.* **2016**, *113*, 8939–8944.
- (30) Place, E.; Evans, N.; Stevens, M. Complexity in biomaterials for tissue engineering. *Nat. Mater* **2009**, *8*, 457–470.
- (31) Carraher, C. L.; Schwarzbauer, J. E. Regulation of Matrix Assembly through Rigidity-dependent Fibronectin Conformational Changes. *J. Biol. Chem.* **2013**, 288, 14805–14814.